

## Curvature of Magnetic Field Lines in Compressible Magnetized Turbulence: Statistics, Magnetization Predictions, Gradient Curvature, Modes, and Self-gravitating Media

Ka Ho Yuen<sup>1</sup> and Alex Lazarian<sup>1,2</sup>

Department of Astronomy, University of Wisconsin-Madison, Madison, WI 53706 USA; kyuen@astro.wisc.edu, alazarian@facstaff.wisc.edu Korea Astronomy and Space Science Institute, Daejeon 34055, Republic of Korea Received 2020 February 4; revised 2020 May 4; accepted 2020 May 13; published 2020 July 24

#### **Abstract**

Magnetic field lines in interstellar media have a rich morphology, which could be characterized by geometrical parameters such as curvature and torsion. In this paper we explore the statistical properties of magnetic field line curvature  $\kappa$  in compressible magnetized turbulence. We see that both the mean and standard deviation of magnetic field line curvature obey power-law relations to the magnetization. Moreover, the power-law tail of the curvature probability distribution function is also proportional to the Alfvénic Mach number. We also explore whether the curvature method could be used in the field-tracing velocity gradient technique. In particular, we observe that there is a relation between the mean and standard deviation of the curvature probed by velocity gradients to  $M_A$ . Finally, we discuss how curvature is contributed by different MHD modes in interstellar turbulence and suggests that the eigenvectors of MHD modes could be possibly represented by the natural Frenet–Serret frame of the magnetic field lines. We discuss possible theoretical and observational applications of the curvature technique, including the extended understanding on a special length scale that characterizes the importance of magnetic field curvature in driving MHD turbulence, and how it could be potentially used to study a self-gravitating system.

Unified Astronomy Thesaurus concepts: Interstellar medium (847); Interstellar magnetic fields (845); Interstellar dynamics (839)

#### 1. Introduction

Turbulence is ubiquitous in astrophysical environments, and the interstellar gases are permeated by turbulent magnetic fields. Magnetohydrodynamic (MHD) turbulence plays a very important role in various astrophysical phenomena (see Armstrong et al. 1995; Biskamp 2003; Elmegreen & Scalo 2004; McKee & Ostriker 2007; Chepurnov & Lazarian 2010; Beresnyak & Lazarian 2019), including star formation (see Mac Low & Klessen 2004; McKee & Ostriker 2007; Fissel et al. 2016), propagation and acceleration of cosmic rays (see Jokipii 1966; Chandran 2000; Farmer & Goldreich 2004; Yan & Lazarian 2008; Lazarian & Yan 2014; Lazarian 2016; Xu & Lazarian 2018), and regulating heat and mass transport between different interstellar medium (ISM) phases (Green 1993; Deshpande et al. 2000; Dickey et al. 2001; Lazarian & Pogosyan 2004, 2006; Khalil et al. 2006; Begum et al. 2006; Padoan et al. 2006 see Draine 2009 for the list of the phases).

The anisotropy of MHD turbulence is being well studied in a number of important theoretical papers (Montgomery & Turner 1981; Matthaeus et al. 1983; Shebalin et al. 1983; Higdon 1984). The study of the MHD turbulence of the solar wind is presented in, e.g., Tu & Marsch (1995) and Goldstein et al. (1995) (see Bruno & Carbone 2013 for a review). The attempts in estimating the anisotropy from observations of the magnetosphere and solar wind resulted in the development of the model of MHD turbulence (see Zank & Matthaeus 1992 and references therein) that incorporates the concept of 2D "reduced MHD" perturbations consisting of 2D "reduced MHD" perturbations carrying approximately 80% of energy and the "slab" Alfvénic waves carrying the remaining 20% of energy (see Matthaeus et al. 2002 and references therein).

The theoretical description of incompressible MHD turbulence that corresponds to numerical simulations was achieved through understanding of both "critical balance" that governs the turbulent motions in the strong turbulence regime Goldreich & Sridhar (1995)<sup>3</sup> and the role of turbulent reconnection that is part and parcel of the turbulent cascade in Lazarian & Vishniac (1999). Goldreich & Sridhar (1995) predicted that most of the Alfvénic energy is concentrated in the modes with critical balance between the parallel and perpendicular motions leading to the scale-dependent anisotropy of the turbulent motions. This anisotropy was derived in Goldreich & Sridhar (1995) in the mean magnetic field of reference and formulated in terms of scaling relation for the wavenumbers  $k_{\parallel} \propto k_{\perp}^{2/3}$ , with  $k_{\parallel,\perp}$  being the parallel and perpendicular wavenumbers, respectively. Later research corrected this point by introducing the local system of reference in which the scale-dependent anisotropy is present. The concept of the local reference system is self-evident from the point of view of turbulent reconnection (see Lazarian et al. 2020 for a review). It was shown in Lazarian & Vishniac (1999) that the magnetic reconnection happens over one eddy turnover time, and therefore Alfvénic turbulence can be presented as the collection of eddies with their angular velocities aligned with the magnetic field. Naturally, this field is not the mean magnetic field, but the field that surrounds the eddy, i.e., the local magnetic field.<sup>4</sup> Therefore, the turbulence scaling should be studied with respect to the local system of reference.

In Goldreich & Sridhar (1995) the insight by Higdon (1984) in terms of magnetized interstellar turbulence was called "nothing short of prophetic." In addition, the Goldreich & Sridhar (1995) study acknowledges that that the "critical balance" between parallel and perpendicular timescales is the key assumption in the derivation of the Straus & Schulz (1976) equations that was claimed in Montgomery (1982) to describe the anisotropic state of incompressible MHD turbulence. Nevertheless, unlike Goldreich & Sridhar (1995), the aforementioned papers did not make the final step and did not provide the derivation of the spectra and the parallel and perpendicular scales.

Incidentally, the critical balance condition in this formulation is a trivial relation between the period of the eddy turnover  $\lambda_{\perp}/v_l$  and the period of the Alfvén wave that the rotation of the eddy induces, i.e.,  $\lambda_{\parallel}/V_{\rm A}$ .

The practical way of defining the local system of reference in numerical simulations was suggested first in Cho & Vishniac (2000), and this and subsequent numerical studies unambiguously confirmed that the critical balance exists only for the eddies, for which parallel and perpendicular scales are measured with respect to the local magnetic field and not with respect to the mean magnetic field (Cho & Vishniac 2000; Maron & Goldreich 2001; Cho et al. 2002). To reflect this in the formulating of MHD theory, the anisotropy is given as a relation between the sizes of parallel and perpendicular eddies given by  $\lambda_{\parallel} \sim \lambda_{\perp}^{2/3}$ , which substitutes the relation between the wavevectors k in the original formulation of the critical balance. The scales  $\lambda_{\perp}$  and  $\lambda_{\parallel}$  are different from reciprocals of  $k_{\perp}$  and  $k_{\parallel}$ , as they are measured in different systems of reference.

Further studies allowed us to extend the original incompressible MHD theory to compressible media (Cho et al. 2002; Cho & Lazarian 2002; Jungyeon & Lazarian 2003; Kowal & Lazarian 2010). A detailed discussion of the theory of turbulence with derivations of the scaling relations and the discussion of the stages of the theory development can be found in reviews (Brandenburg & Lazarian 2013; Beresnyak et al. 2005) and in a recent monograph on MHD turbulence (Beresnyak & Lazarian 2019).

The geometry of magnetic field is also a very important way to characterize its importance in interstellar turbulent media. The Cauchy momentum equation carries a force term that is proportional to  $\mathbf{B} \times (\nabla \times \mathbf{B})$ , where  $\mathbf{B}$  is the magnetic field, which could be decomposed into the pressure term  $\nabla(\mathbf{B}^2)$  and the tension term  $\tilde{\mathbf{B}} \cdot \nabla \mathbf{B}$  (see Biskamp 2003). The former term drives compression of fluid elements, while the latter term contains information on how magnetic field bending would introduce acceleration to fluid elements. If the magnetic field lines, with their strength being constant, are bent with a curvature  $\kappa$ , then the tension term would be proportional to  $\kappa \mathbf{B}^2$ . Therefore, characterizing the magnetic field curvature in MHD turbulence allows one to directly estimate how much force the magnetic field bending exerts on fluid elements.

Curvature of magnetic field could also estimate the magnetization. The curvature method has a significant advantage compared to the traditional magnetic field polarization dispersion method, in that the latter only gives an estimation of  $M_A$  in a statistical area. For interstellar media that have force balances within, the curvature of magnetic field is expected to have a proportionality to magnetic field of  $B^{-2}$ , which reflects the force balance that is employed by the technique in Li et al. (2015) that yields results consistent with the Chandrasekhar & Fermi (1953) technique. Notice that the curvature of magnetic field is a local quantity, while the method of dispersion could only be measured statistically within a selected region, which could provide a significant advantage in characterizing the field strength with higher-resolution data.

This paper investigates the curvature of magnetic field lines in the case of balanced turbulence. We start by introducing the theoretical formulation of curvature of a magnetic field line in MHD turbulence, as well as the expectation of curvature dependencies on magnetic field strength in terms of MHD turbulence theory. In Section 2 we discuss the numerical method and introduce an efficient curvature calculation algorithm applicable both numerically and observationally. In Section 4 we discuss the statistics on magnetic field line curvature, especially on how it is related to both magnetization and magnetic field strength, both 3D and 2D. In Section 5 we discuss the potential use of the curvature of velocity gradients in estimating the field strength. In Section 6 we discuss how the three MHD modes behave both theoretically and numerically when there is a nonzero curvature in magnetic field lines, and we discuss the length scales at which curvature would drive the MHD modes. In Section 8 we discuss the potential use and caveats of the curvature method. In particular, we discuss how curvature would possibly deduce gravitational status in Section 8.4. In Section 9 we conclude our paper.

### 2. The Theory of Magnetic Field Line Curvature

# 2.1. Mathematical Formulation of Curvature and Torsion of Magnetic Field Lines

The magnetic field line can be considered to be "the path" of an imaginary particle with the particle speed B at each point in a small neighborhood. Such characterization of "magnetic field lines" globally does not exist since the concept of magnetic field lines becomes ambiguous when we face regions with magnetic reconnections or magnetic field crossing (Newcomb 1958). The consideration of the geometry of the local field lines provides an immediate advantage: a natural curvilinear frame called the Frenet-Serret frame could be defined locally with two geometric properties about magnetic field called curvature  $\kappa$  and torsion  $\tau$ , which characterize how the magnetic field lines deviate from a line and a plane, respectively. While their velocity counterparts (velocity curvature, torsion) are well studied (see, e.g., Braun et al. 2006; Kadoch et al. 2011), the study of magnetic field curvature has not been popular until recently (Yang et al. 2019).

In the studies of magnetic field topology, the concept of curvature is important since magnetic field lines are expected to have a smaller curvature as the strength of the magnetic field increases. A recent numerical work by Yang et al. (2019) shows the probability density function (pdf) of the magnetic field curvature has a power-law tail of  $\kappa^{-2}$  in 2D and  $\kappa^{-2.5}$  in 3D for incompressible simulation with initially fluctuation energy equipartitioned between the kinetic and magnetic ones. They also show that magnetic field lines follow a proportionality relation of  $\kappa \propto f_B/B^2$ , where  $f_b$  represents the normal force component. Observationally Li et al. (2015) use the curvature of magnetic field lines as an estimate of magnetic field strength in NGC 6334. Together, curvature of magnetic field lines becomes an important physical quantity in characterizing the strength of magnetic field.

Mathematically, we would parameterize the magnetic field lines by the line variable s assuming that the magnetic field forms a vector field for an imaginary particle. Intuitively, we would imagine a particle placed at at an arbitrary initial position  $\mathbf{r}_0$  and allow it to evolve following the vector integral  $\frac{d\mathbf{L}_B}{dt} = \mathbf{B}(\mathbf{r} - \mathbf{r}_0)$ , where the magnetic field  $\mathbf{B}$  is a velocity field

 $<sup>\</sup>overline{}^5$  We note that in the frame of the mean magnetic field the anisotropy is different, i.e.,  $k_{\parallel} \sim C k_{\perp}$ , where C is a constant, i.e., there is no anisotropy that changes with the scale (see Cho et al. 2002). For historic reasons, due to the original formulation in the pioneering Goldreich & Sridhar (1995) study, this fact sometimes causes confusion with the researchers searching the scale-dependent anisotropy measuring parallel and perpendicular direction with respect to the mean magnetic field.

of the particle. The path length of the imaginary particle is then

$$s(l) = \int_0^l dl' \sqrt{B_x^2(l') + B_y^2(l') + B_z^2(l')}, \tag{1}$$

and the Frenet–Serret frame of the magnetic fields lines would be (Callen et al. 2003)

$$\frac{d\hat{t}}{ds} = +\kappa \hat{n}$$

$$\frac{d\hat{n}}{ds} = -\kappa \hat{t} + \tau \hat{b}$$

$$\frac{d\hat{b}}{ds} = -\tau \hat{n},$$
(2)

where  $\hat{t} = \hat{B}$  is the unit vector of the magnetic field,  $\hat{n}$ ,  $\hat{b}$  are the normal and binormal vectors, respectively,  $\frac{dx}{ds} = \hat{t} \cdot \nabla x$  is the line derivative along a vector x, and  $\tau$  is the torsion of the magnetic field line (Section 8.1). Under this formulation, the signed curvature could be given by

$$\kappa = \hat{n} \cdot \frac{d\hat{t}}{ds}.\tag{3}$$

### 2.2. Prediction of Dependencies of Curvature on Magnetic Field Strength and Sonic and Alfvénic Mach Number in MHD Turbulence

The Frenet–Serret frame is a natural frame in studying the local geometry of magnetic field. We expect that in the presence of magnetized turbulence, there should be a power law  $\kappa \propto B^{-\gamma}$ , where  $\gamma$  is a constant yet to be defined. From Equation (3), apparently the magnetic field line curvature is inversely proportional to the squared amplitude of magnetic field. Indeed, as argued in Yang et al. (2019), if the force term is constant, then  $\kappa \propto B^{-2}$ , but in the case of MHD turbulence the interaction of velocity and magnetic fields would tend to reduce the dependencies of  $\kappa$  to B. Therefore, we would expect the properties of turbulence are characterized not only by magnetic field strength but also by the velocities and densities of the fluid elements, a more appropriate estimate would be

$$\kappa \propto M_{\rm A}^{\gamma},$$
 (4)

where  $M_{\rm A} = v_{\rm inj}/v_{\rm A}$  is the ratio of the injection and Alfvén velocities,  $v_{\rm A} = B_0/\sqrt{4\pi\rho_0}$ .

We can make a similar estimation on the dependence of  $\kappa \propto M_A^{\gamma}$  from the theory of MHD turbulence (Goldreich & Sridhar 1995; Lazarian & Vishniac 1999). As Goldreich & Sridhar (1995) formulated for trans-Alfvénic, i.e.,  $M_A=1$  turbulence, in what follows we are mostly using the Lazarian & Vishniac (1999) expressions obtained for  $M_A<1$ . For  $M_A>1$  the Goldreich & Sridhar (1995) approach can be easily generalized (see Lazarian 2006) as we discuss below.

In the incompressible limit, the parallel and perpendicular length scales of the turbulent eddies would be related by the following relations based on the theory of MHD turbulence. In the following we shall only consider cases where we have strong magnetic field  $(M_A = v_{\rm inj}/v_A < 1)$ , where  $v_{inj}$  is the injection velocity and  $v_A$  is the Alfvén velocity) or we are in the regime of dynamically important magnetic field  $(M_A > 1)$  but the length scale  $l < l_A = L_{\rm inj} M_A^{-3}$ , where  $L_{inj}$  is the injection scale). Here we consider that the magnetic field eddies that are coherent to that of the velocity eddies (which is the case when

we are considering Goldreich & Sridhar turbulence; see Goldreich & Sridhar 1995), so that one could simply use the same scaling law for magnetic field structures without further approximations.

In the cases of strong magnetization, there exists a scale  $l = L_{\rm ini} M_{\rm A}^2$  such that scales smaller than that would be the strong turbulence. We shall omit discussion of length scales larger than that since those usually have a limited spatial range. We stress that the parallel length scale  $\lambda_{\parallel}$  and perpendicular length scale  $\lambda_{\perp}$  are defined in terms of the *local* direction of magnetic field. While in earlier works (Shebalin et al. 1983; Higdon 1984; Matthaeus et al. 1996) the anisotropy is observed and theoretically tested, these anisotropies are generally measured along the mean magnetic field. In fact, the concept of the local magnetic field is absent in Goldreich & Sridhar (1995), where all the closure relations used for the derivation are formulated in the reference frame of the mean field (Lazarian & Vishniac 1999). The concept of local reference frame was shown to be valid numerically (see Cho & Vishniac 2000; Maron & Goldreich 2001; Cho et al. 2001, or the Appendix of Lazarian et al. 2018 for a comprehensive discussion). It is important to stress that the relations between  $\lambda_{\parallel}$  and  $\lambda_{\perp}$  are *not valid* if  $\parallel$  and  $\perp$  distances are measured with respect to the mean field (Cho & Vishniac 2000).

Notice that the Goldreich-Sridhar turbulence has to be understood under the reference frame defined by the local magnetic field directions (Lazarian & Vishniac 1999; Lazarian et al. 2018). That means that the anisotropy should be computed with respect to magnetic field at the scale of the eddies. In the local system of magnetic field of the eddies, the parallel and perpendicular scales of the eddies are related for  $M_A < 1$  as (Lazarian & Vishniac 1999)

$$\lambda_{\parallel} \sim L_{\rm inj} \left( \frac{\lambda_{\perp}}{L_{\rm inj}} \right)^{2/3} M_{\rm A}^{-4/3},$$
 (5)

where  $\lambda_{\parallel,\perp}$  are the parallel and perpendicular length scales of the turbulent eddies under Lazarian & Vishniac (1999) formalism. Equation (5) has two differences from the original expression by Goldreich & Sridhar (1995). First of all, it relates the physical scales of the eddies rather than wavenumbers. The latter are given in the frame of the mean field and do not exhibit the scale-dependent anisotropy of Equation (5). Second, Goldreich & Sridhar theory is formulated for  $M_A=1$ .

Readers should be careful that the parallel and perpendicular scales that we are discussing here are referring to the local scales argument in Lazarian & Vishniac (1999). Numerically the 2/3 scaling law is tested in Cho & Vishniac (2000), and the energy spectrum is tested in Jungyeon & Lazarian (2003). Those studies confirmed that the aspect ratio is larger for smaller eddies and, in fact, follows the predicted "critical balance" relation. The justification of such a procedure follows from the eddy description of MHD turbulence based on the Lazarian & Vishniac (1999) study. The subsequent studies (see Cho et al. 2002; Beresnyak et al. 2005) provided the numerical support for these scalings. Recently, Yuen et al. (2018, see their Appendix) also revisited this issue and stated again clearly that only the local computation would yield the desired 2/3 scaling law, in agreement with the expectations based on Lazarian & Vishniac (1999) reconnection theory.

For super-Alfvénic turbulence  $\dot{M}_{\rm A} > 1$  and at large scales magnetic fields do not change the Kolmogorov picture. In the

case of weak magnetization and  $l < l_{\rm A} = L_{\rm inj} M_{\rm A}^{-3}$ , the parallel length scale  $\lambda_{\parallel}$  and perpendicular length scale  $\lambda_{\perp}$  are related by

$$\lambda_{\parallel} \sim L_{
m inj} \left(rac{\lambda_{\perp}}{L_{
m inj}}
ight)^{2/3}.$$
 (6)

In either case, the *minimal* curvature of the eddies measured for the eddy of size  $\lambda_{\perp}$  could be estimated by  $\lambda_{\perp}/\lambda_{\parallel}^2$ . Therefore, we would obtain the expected curvature for eddies as a variable of the minor length  $\lambda_{\perp}$ :

$$\kappa(\lambda_{\perp}) \sim L_{\text{inj}}^{-2/3} \lambda_{\perp}^{-1/3} 
\cdot \begin{cases}
M_{\text{A}}^{8/3} & (M_{\text{A}} < 1, l < L_{\text{inj}} M_{\text{A}}^{2}) \\
1 & (M_{\text{A}} > 1, l < L_{\text{inj}} M_{\text{A}}^{-3}),
\end{cases} (7)$$

for which the curvature at length scale  $\lambda_{\perp}$  is proportional to the Alfvénic Mach number. Here the curvature that we measured,  $\kappa(\lambda_{\perp})$ , corresponds to the curvature we measure in real space when we only discuss eddies of size  $\lambda_{\perp}$ . For eddies larger than the scales in the two individual cases, i.e., for  $l > L_{\rm inj} M_{\rm A}^2$  if  $M_{\rm A} < 1$  and  $l < L_{\rm inj} M_{\rm A}^{-3}$  for  $M_{\rm A} > 1$ , the curvature of these isotropic eddies with scale  $\lambda$  is simply  $\lambda^{-1}$  with no relation between  $\lambda$  and  $M_{\rm A}$ .

The measured curvature value in real space would be mainly contributed by two factors: (1) the largest scale that has turbulent anisotropy and (2) contributions from eddies with scales larger than the largest scale that has turbulent anisotropy. Since the curvature value of real space is basically a statistical sum of all curvature values from the eddies with different sizes, it is natural to consider for what size the eddy dominates over the measurements. In the case of sub-Alfvénic turbulence, the largest scale measurable with anisotropy is  $l = L_{\rm inj} M_{\rm A}^2$ . Therefore, the curvature of eddies at scale  $l = L_{\rm inj} M_{\rm A}^2$  would be

$$\kappa(\lambda_{\perp} = L_{\rm inj} M_{\rm A}^2) = L_{\rm inj}^{-1} M_{\rm A}^2 \quad (M_{\rm A} < 1),$$
 (8)

while for super-Alfvénic turbulence, the respective transition scale is  $l = L_{\rm inj} M_{\rm A}^{-3}$ ,

$$\kappa(\lambda_{\perp} = L_{\rm inj} M_{\rm A}^{-3}) = L_{\rm ini}^{-1} M_{\rm A}^{\rm l} \quad (M_{\rm A} > 1).$$
(9)

The contribution of curvature from eddies with scales larger than the scale having turbulence anisotropy has no dependence on  $M_A$ . The observed curvature would then be a statistical sum of curvature values acting on different size of eddies. Moreover, notice that the discussion above is based on the turbulence scaling laws from incompressible turbulence theory. Since compressible modes in compressible magnetized turbulence (see Jungyeon & Lazarian 2003) rarely have nonzero curvature and the observed curvature is the statistical average of the curvature values obtained from the three MHD modes, the larger weight of compressible modes would decrease the observed curvature (see discussion in Section 6). Observationally we cannot perform an analysis of curvature as a function of  $\lambda_{\perp}$  unless precise magnetic field orientations are given, which requires the knowledge of the 3D magnetic field distribution. Statistically one would only obtain a value of curvature contributed by all three modes of MHD turbulence and all scales. As a result, we expect that the measured curvature value

Table 1
Description of MHD Simulation Cubes, Some of Which Have Been Used in the Series of Papers about VGT (Yuen & Lazarian 2017a, 2017b; Lazarian & Yuen 2018a, 2018b)

Model	$M_S$	$M_A$	$\beta = 2M_{\rm A}^2/M_{\rm S}^2$	Resolution
huge-0	6.17	0.22	0.0025	792 <sup>3</sup>
huge-1	5.65	0.42	0.011	$792^{3}$
huge-2	5.81	0.61	0.022	$792^{3}$
huge-3	5.66	0.82	0.042	$792^{3}$
huge-4	5.62	1.01	0.065	$792^{3}$
huge-5	5.63	1.19	0.089	$792^{3}$
huge-6	5.70	1.38	0.12	$792^{3}$
huge-7	5.56	1.55	0.16	$792^{3}$
huge-8	5.50	1.67	0.18	$792^{3}$
huge-9	5.39	1.71	0.20	$792^{3}$

**Note.**  $M_s$  and  $M_A$  are the rms values at each snapshot.

has a weaker dependence on  $M_A$  for both cases, i.e., we expect

$$\kappa \sim L_{\rm inj}^{-1} \cdot \begin{cases} M_{\rm A}^{2-\alpha} & (M_{\rm A} < 1) \\ M_{\rm A}^{1-\alpha} & (M_{\rm A} > 1) \end{cases}$$
 (10)

for some constant  $\alpha$  dependent on the properties of injection and the composition of modes. As we will see in Section 4, the inclusion of  $\alpha$  is necessary in explaining the behavior of curvature in compressible turbulence.

We also expect the index  $\gamma = 2 - \alpha(M_A < 1)$  or  $1 - \alpha(M_A > 1)$  to be shallower in 2D, i.e  $\gamma_{2D} < \gamma_{3D}$  since the projection effect of magnetic field would tend to cancel out the magnetic field deviations, which are not a straight line. As a result, the curvature observed in the projected space should be systematically smaller than that in 3D.

### 3. Method

#### 3.1. Simulation Setup

The numerical data cubes are obtained by 3D MHD simulations that are from a single-fluid, operator-split, staggered grid MHD Eulerian code ZEUS-MP/3D to set up a 3D, uniform turbulent medium. Our simulations are isothermal with  $T=10\,\mathrm{K}$ . To simulate the part of the interstellar cloud, periodic boundary conditions are applied. We inject turbulence solenoidally.

For our controlling simulation parameters, various Alfvénic Mach numbers  $M_A = V_{\rm inj}/V_A$  and sonic Mach numbers  $M_s = V_{\rm inj}/V_s$  are employed, where  $V_{\rm inj}$  is the injection velocity, while  $V_A$  and  $V_s$  are the Alfvén and sonic velocities, respectively, which are listed in Table 1. For the case of  $M_A < M_s$ , it corresponds to the simulations of turbulent plasma with thermal pressure smaller than the magnetic pressure, i.e., plasma with low confinement coefficient  $\beta/2 = V_s^2/V_A^2 < 1$ .

These simulations are the Fourier-space forced driving isothermal simulations. The choice of force stirring over the other popular choice of decaying turbulence is because only the former will exhibit the full characteristics of turbulence statistics (e.g., power law, turbulence anisotropy) extended from k=2 to a dissipation scale of 12 pixels in a simulation, which matches with what we see in observations (e.g., Armstrong et al. 1995; Chepurnov & Lazarian 2010).

<sup>&</sup>lt;sup>7</sup> For isothermal MHD simulation without gravity, the simulations are scale-free. The two scale-free parameters  $M_A$ ,  $M_s$  determine all properties of the numerical cubes, and the resultant simulation is universal in the inertial range. That means that one can easily transform to whatever units as long as the dimensionless parameters  $M_A$ ,  $M_s$  are not changed.

In contrast, the case  $M_A > M_s$  corresponds to the magnetic-pressure-dominated plasma with high confinement coefficient  $\beta/2 > 1$ .

From now on we refer to the simulations in Table 1 by their model name. For example, the figures with model name indicate which data cube was used to plot the corresponding figure. Each simulation name follows the rule that is the name is with respect to the varied  $M_s$  and  $M_A$  in ascending order of confinement coefficient  $\beta$ . The selected ranges of  $M_s$ ,  $M_A$ , and  $\beta$  are determined by possible scenarios of astrophysical turbulence from very subsonic to supersonic cases.

### 3.2. Synthetic Observations

The raw data from simulation cubes are converted to synthetic maps for studies of curvature. Since we would investigate both polarization and magnetic field probed by the velocity gradient technique (VGT; Yuen & Lazarian 2017a; Lazarian & Yuen 2018a, see Section 3.3), we shall deliver the method of synthesizing the Stokes parameters, intensities, centroids, and velocity channels here.

The Stokes parameters for synthetic observation are given by

$$Q \propto \int dz n \cos(2\theta) \sin^2 \gamma_{\rm inc}$$

$$U \propto \int dz n \sin(2\theta) \sin^2 \gamma_{\rm inc}$$

$$\theta_{\rm pol} = \frac{1}{2} \tan 2^{-1} (U/Q), \tag{11}$$

where n is the number density and  $\theta$  and  $\gamma_{\rm inc}$  are the 3D planer angle and inclination angle of magnetic field vectors with respect to the line of sight (LOS), respectively. The dispersion of the polarization angle  $\theta_{pol}$  is directly proportional to the perpendicular Alfvénic Mach number  $M_{A,\perp}$ .

The normalized velocity centroid  $C(\mathbf{R})$  in the simplest case<sup>8</sup> is defined as

$$C(\mathbf{R}) = I^{-1} \int \rho_{\nu}(\mathbf{R}, \nu) \nu d\nu,$$

$$I(\mathbf{R}) = \int \rho_{\nu}(\mathbf{R}, \nu) d\nu,$$
(12)

where  $\rho_{\nu}$  is density of the emitters in the position–position–velocity (PPV) space,  $\nu$  is the velocity component along the LOS, and  $\boldsymbol{R}$  is the 2D vector in the pictorial plane. The integration is assumed to be over the entire range of  $\nu$ . Naturally,  $I(\boldsymbol{R})$  is the emission intensity. C(R) is also an integral of the product of velocity and LOS density, which follows from a simple transformation of variables (see Lazarian & Esquivel 2003). For constant density, C(R) is just the LOS velocity averaged over the LOS.

We also consider the velocity channel at v=0 here as a case study. Mathematically, the density in PPV space of emitters with local sonic speed  $c_s(\mathbf{x}) = \sqrt{\gamma k_B T / \mu_{\text{MMW}}}$ , where  $\mu_{MMW}$  is the mean molecular weight of the emitter, moving along the LOS with stochastic turbulent velocity  $u(\mathbf{x})$  and regular coherent velocity, e.g., the galactic shear velocity,  $v_g(\mathbf{x})$ , is

(Lazarian & Pogosyan 2004)

$$\rho_s(X, v) = \int_0^S dz \frac{\rho(x)}{\sqrt{2\pi\beta_T}} \exp\left[-\frac{(v - v_g(x) - u(x))^2}{2c_s^2(X, z)}\right],$$
(13)

where sky position is described by 2D vector X = (x, y), z is the LOS coordinate,  $\gamma$  is the adiabatic index, and S is the cloud depth. Notice that  $c_s$  would be a function of distance if the emitter is not isothermal. Equation (13) is *exact*, including the case when the temperature of emitters varies in space. The observed velocity channel at velocity position  $v_0$  and channel width  $\Delta v$  is then, assuming a constant velocity window W(v) = 1 and  $v_o(x) = 0$ ,

$$Ch(X; v_0, \Delta v) = \int_{v_0 - \Delta v/2}^{v_0 + \Delta v/2} dv \rho_s(X, v)$$

$$= \int_0^S dz \frac{\rho(x)}{\sqrt{2\pi c_s^2}} \int_{v_0 - \Delta v/2}^{v_0 + \Delta v/2} dv e^{-\frac{(v - u(x))^2}{2c_s^2}}.$$
(14)

We shall deliver the method of computing the gradients of velocity channel and use it as a probe of tracing magnetic fields.

#### 3.3. Velocity Gradient Technique

The VGT (see González-Casanova & Lazarian 2017) is an innovative method that uses the properties of turbulence anisotropy in MHD turbulence to probe the direction of magnetic field. The basic idea is to obtain the magnetic field predictions by rotating the output of the sub-block averaging of the gradients of observables by 90° (Yuen & Lazarian 2017a), which is supported by a number of theoretical and numerical works (Goldreich & Sridhar 1995; Lazarian & Vishniac 1999; Maron & Goldreich 2001; Cho & Lazarian 2002; Jungyeon & Lazarian 2003) The VGT is applicable to velocity centroids (González-Casanova & Lazarian 2017; Yuen & Lazarian 2017a), intensities (Yuen & Lazarian 2017a; Hu et al. 2019), and also velocity channel maps (Lazarian & Yuen 2018a). The same method is also migrated to synchrotron studies and applicable to both synchrotron intensities (Lazarian et al. 2017) and multifrequency synchrotron polarization (Lazarian & Yuen 2018b).

The gradients of the three observables (intensity, centroid, velocity channel) we introduced in Section 3.2 would be computed as follows. We would first compute the Sobel kernel of the observables, which we would call the raw gradients. The distribution histogram peak of raw gradients would provide us with the predicted direction of magnetic field directions probed by the gradients of observables, provided that the Gaussian fitting requirement stated in Yuen & Lazarian (2017a) is satisfied, which is called sub-block averaging in Yuen & Lazarian (2017a). The 90° rotated gradients are our predicted magnetic field directions by the gradients of observables. We would not apply further improvements of the technique (e.g., Hu et al. 2018; Lazarian & Yuen 2018a) since these techniques tend to straighten the estimated magnetic field lines.

<sup>&</sup>lt;sup>8</sup> Higher-order centroids are considered in Yuen & Lazarian (2017b), and they have  $v^n$ , e.g., with n = 2, in the expression of the centroid. Such centroids may have their own advantages. However, for the sake of simplicity we employ for the rest of the paper n = 1.

## 3.4. Self-consistent Curvature and Torsion Obtaining Method through Enumerating Lagrangian Particles

Computing curvature by Equation (2) is difficult since the computation of  $\mathbf{B} \cdot \nabla \mathbf{B}$  does not often yield a vector parallel to  $\hat{n}$  numerically. The reason is that the spatial derivative of magnetic field is not guaranteed to have  $(\mathbf{B} \cdot \nabla \mathbf{B}) \cdot \mathbf{B} = 0$ . In view of that, Yang et al. (2019) use the expression  $\kappa = |\hat{\mathbf{B}} \times (\hat{\mathbf{B}} \cdot \nabla \hat{\mathbf{B}})|$  to extract the curvature-only part of magnetic field. Below we discuss an algorithm that could possibly bypass the problem with the cost of interpolation accuracy: we treat the magnetic field as the velocity field of an imaginary particle (see Section 2) and find the path integral in a sufficiently small area, so that one could have a representation of the "magnetic field line function  $L_{\mathcal{B}}(t)$ " that has

$$L_B(t=0) = r_0$$
 = Spatial position of the pixel 
$$\frac{dL_B}{dt} = B(r - r_0). \tag{15}$$

Readers should be reminded that if we put  $\frac{dL_B}{dt} = v$ , then we are effectively converting the Eulerian hydrodynamic variables to the Lagrangian one, which is simply the standard Lagrangian particle-tracking algorithm (see Ouellette et al. 2006; Xu et al. 2007).

We perform an integrator method that integrates Equation (15) by the Runge-Kutta method (order 2/4/4.5 depending on the accuracy requirement). See the Appendix for the convergence test. We first impose an interpolation field so that the magnetic vector field  $\boldsymbol{B}(\boldsymbol{r})$  is well defined in a local patch of the 3D real space  $\boldsymbol{r} \in \Delta L^3 \subset \mathbb{R}^3$ . The interpolation is usually performed using the family of splines to estimate values between the grid points. Cubic spline is a popular option. The interpolation could be done very easily through Julia's Interpolation package. Then, one could obtain the tangent vector:

$$T(t) = \frac{\dot{L}_B(t)}{|\dot{L}_B(t)|}. (16)$$

Following Equation (3), one could obtain both  $\kappa$  and  $\tau$  very easily.

The number of steps required for the integrator method is explicitly dependent on how one expresses the differential operator  $\frac{d}{dt}$ . For instance, if one uses the 1D five-point stencil in estimating the differentiation on the position vector  $\mathbf{r}(t)$  at time  $t_0$  with some custom step size dt,

$$r'(t_0) = \frac{-r(t_0 + 2dt) + 8r(t_0 + dt) - 8r(t_0 - dt) + r(t_0 - 2dt)}{12dt}$$
(17)

then the number of points required in obtaining  $\kappa(t=t_0)$  and  $\tau(t=t_0)$  (see Section 8.1) at position  $t_0$  is  $2 \times (5-1) + 1 = 9$  and  $3 \times (5-1) + 1 = 13$  points, respectively. The advantage of the current method is that we are sticking to the definition of the Frenet–Serret frame based on the tangent of the (magnetic field) line. The small dt will guarantee that the integrated line would only be locally defined. The method is valid for both 2D and 3D. However, readers should be

reminded that torsion is nonzero only when we are tackling a 3D line.

This method is very versatile since one could also compute curvature of scalar structures, say, intensity map I, by replacing B in Equation (15) with the gradients of I rotated by 90°. This application is especially useful for the studies based on the VGT since curvature is an important quantity aside from orientation and amplitudes of gradients that characterize the underlying magnetic field properties.

Readers should be reminded that, to compute curvature, one must make sure the respective circle that has radius  $1/\kappa$  could be represented by the grid resolution. One caveat here is that it is impossible to obtain curvature values larger than 0.5 (in units of 1 pixel<sup>-1</sup>) since the respective circle with radius smaller than 2 pixels would not be resolved in the numerical grid.

## 4. Statistical Properties of Magnetic Field Curvature and Torsion in 3D MHD Compressible Turbulence

The very first thing to start with would be to examine the statistical properties of the curvature field. We shall discuss the statistics through the simple tools like mean, standard deviations, and histograms in both 3D and projected 2D spaces and both along and perpendicular to the field lines. Previous works that discuss curvatures are mainly focused on the curvature of velocity fields (Braun et al. 2006; Ouellette & Gollub 2007, 2008; Kadoch et al. 2011). The study of statistics on magnetic field curvature is only recently done by Yang (2019) by an incompressible equipartitioned magnetized turbulence simulation. As commented in Section 2, we expect that the statistical parameters would give us a dependence of  $\kappa \propto M_A^{\gamma}$  for some *positive* values of  $\gamma$ . For the reader's reference, we are expressing the values of  $\kappa$  as the function of numerical pixels since there is an explicit upper bound for  $\kappa$  in numerical simulations (see Section 3.4).

#### 4.1. Curvature of 3D Magnetic Field

In 3D we do not need to employ the algorithm as listed in Section 3.4 since it is straightforward to show  $\kappa = |\hat{\boldsymbol{B}} \times (\hat{\boldsymbol{B}} \cdot \nabla \hat{\boldsymbol{B}})|$ . Figure 1 shows how the 3D statistics would behave as a function of the Alfvénic Mach number. Here we use the mean and standard deviation as ways to extract simple statistics (top panel and middle panel of Figure 1). From our theoretical discussion (Section 2), we expect that statistically the magnetic field curvature should be proportional to  $M_A^{\gamma}$  for some constant  $\gamma$ . From the top panel of Figure 1, we see a two-section power law for  $\langle \kappa \rangle$  (in 1 pixel<sup>-1</sup>):

$$\langle \kappa \rangle \propto \begin{cases} M_{\rm A}^{1.67} & M_{\rm A} < 1 \\ M_{\rm A}^{0.71} & M_{\rm A} \geqslant 1 \end{cases}$$
 (18)

with a turning point  $\langle \kappa \rangle \sim 0.15 \, \mathrm{pixel^{-1}}$ , while for standard deviation of curvature,  $\sigma_{\kappa}$  (middle panel of Figure 1, in 1  $\mathrm{pixel^{-1}}$ ),

$$\sigma_{\kappa} \propto \begin{cases} M_{\rm A}^{1.67} & M_{\rm A} < 1\\ M_{\rm A}^{0.78} & M_{\rm A} \geqslant 1 \end{cases}$$
 (19)

with a turning point  $\langle \kappa \rangle \sim 0.25 \, \text{pixel}^{-1}$ . The fitting lines in Equations (18) and (19) look surprisingly similar, with a

https://github.com/JuliaMath/Interpolations.jl

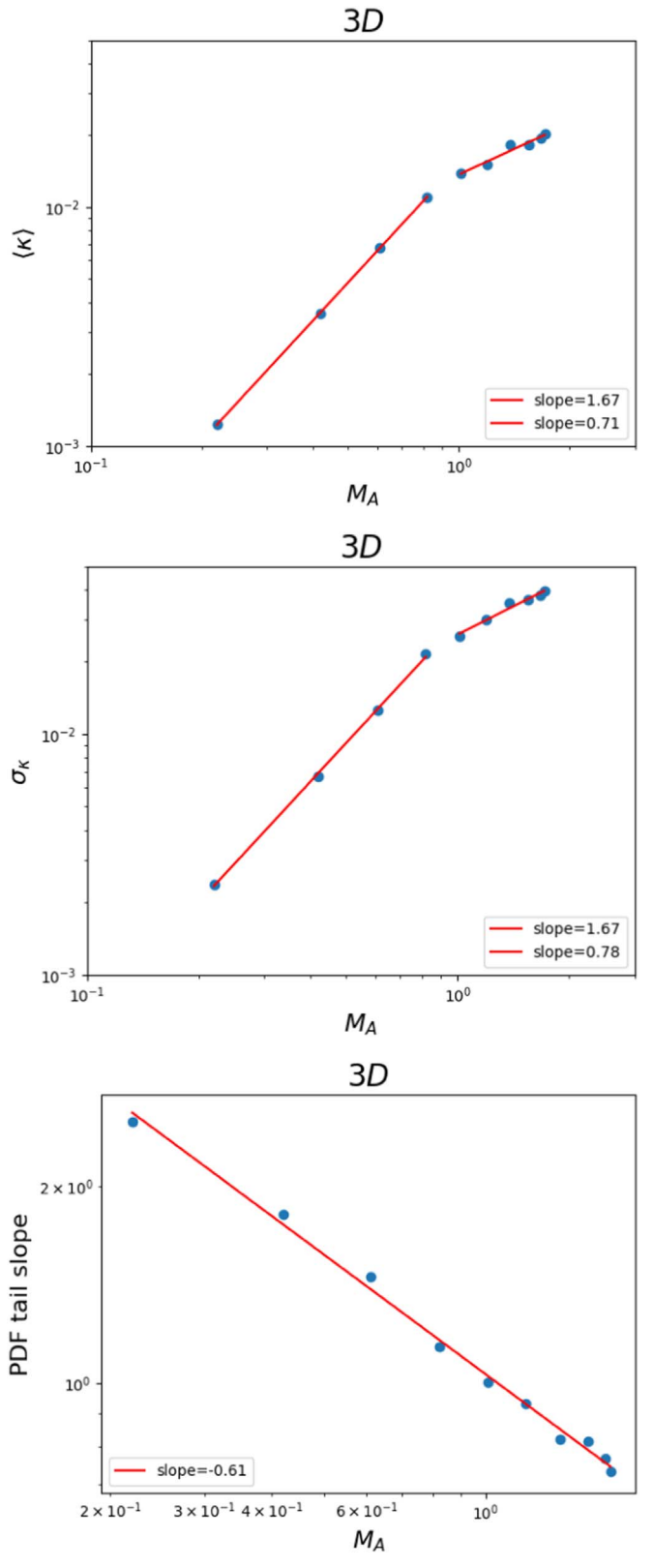


**Figure 1.** Set of figures showing the mean value of curvature  $\langle \kappa \rangle$  (top), the standard deviation of curvature  $\sigma_{\kappa}$  (middle), and the pdf power-law tail slope of the magnetic field curvature  $\kappa$  (bottom) with respect to the Alfvénic Mach number  $M_A$ . Notice that the power-law tail slope is expected to be negative; we are plotting its absolute value.

relatively high coefficient of determination of 0.9 or above. These measurements are consistent with the theoretical prediction in Section 2.2, with the coefficient  $\alpha$  defined in

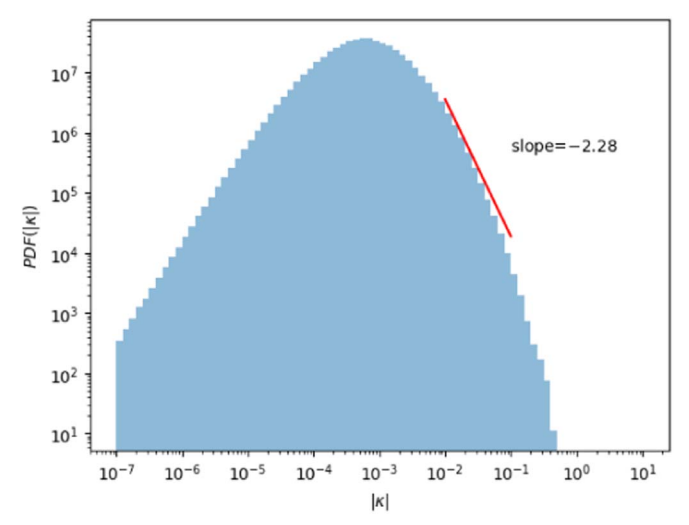


**Figure 2.** The pdf of curvature for the cube huge-0. We see a power-law tail slope of 2.28 for this particular cube, which has a slightly smaller value than the value recently seen in Yang et al. (2019) (2.5).

Section 2.2 to be

$$\alpha = \begin{cases} 0.33 & (M_{A} < 1, \langle \kappa \rangle) \\ 0.29 & (M_{A} > 1, \langle \kappa \rangle) \\ 0.33 & (M_{A} < 1, \sigma_{\kappa}) \\ 0.22 & (M_{A} > 1, \sigma_{\kappa}) \end{cases}$$
(20)

which are fairly similar for these four cases. The split of the power laws between  $M_A \ge 1$  and  $M_A < 1$  is also expected and consistent with our findings in one of our previous works using velocity gradients in probing magnetization (Lazarian et al. 2018) since there are different scaling laws below and above  $M_A$ .

We also employ the method of histogram tails since it was suggested that  $f(\kappa) \sim \kappa^{-2.5}$  in Yang et al. (2019). The bottom panel of Figure 1 shows the power-law tail slope as a function of  $M_A$ . One could see that the slope power-law tail is actually a function of  $M_A$ . Our result (see Figure 2) should not be directly compared to that in Yang et al. (2019), who have a general slope of -2.5 since we are performing simulations for different settings: (1) We are performing full 3D, compressible, driven simulations, while Yang et al. perform 3D, incompressible, decaying simulations. The compressible simulation allows one to store energy in the two other compressible modes, effectively reducing the curvature of magnetic field lines driven by turbulence driving. (2) We are testing our theory using the turbulence statistics, while the work of Yang et al. is based on the formulation of the magnetic force term in the Cauchy momentum equation (3). We tested the dependencies of the histogram tail as a function of global Alfvénic Mach number with multiple simulations, while Yang et al. (2019) characterize the curvature as a distribution of local magnetic field strength. Moreover, it is expected that the pdf of the curvature should be a function of Alfvénic Mach number since in a strongly magnetized medium we do not expect a large variation of curvature values owing to the constraints of a strong field, resulting in a relatively steep power-law tail in the low  $M_A$  limit. In the case of weak magnetic field, the allowed values of curvature are less bounded by the magnetic field itself compared to the strong-field cases, which would lead to an extended pdf tail and a shallower slope.

## 4.2. 2D Magnetic Field Curvature Obtained in Synthetic Observations

We would like to see whether the dependencies would be seen in observation when we view the cloud parallel or perpendicular to the LOS. Figure 3 shows how  $\langle \kappa \rangle$ ,  $\sigma_{\kappa}$ , and the slope of the pdf tail would respond as a function of  $M_A$  when we project the Stokes parameter perpendicular and parallel to the mean magnetic field using the procedure laid out in Section 3.

We immediately recognize that there are different behaviors for the relation of  $\langle \kappa \rangle$  to  $M_A$  in 2D and 3D. In 3D we have a two-section power law that has a cutoff of  $M_A=1$ . However, such a power law is not seen in both cases of  $B \perp$  LOS and  $B \parallel$  LOS. In fact, in the case of  $B \perp$  LOS we see that a uniform power law describes the data better, which has  $\langle \kappa \rangle \propto M_A^{1.17}$ . Nevertheless, it is shallower than the section of the power law that we have in  $M_A < 1$  in Section 4.1 yet steeper than the other section of the power law that we have in  $M_A > 1$ . A very similar effect also happens to  $\sigma_{\kappa}$ , that only a single power law would be sufficient to describe the data here  $(\sigma_{\kappa} \propto M_A^{1.39})$ .

We also see that the previously seen power law disappears when we project the magnetic field data along its mean field direction, i.e.,  $B\|$  LOS. In this scenario both  $\langle\kappa\rangle$  and  $\sigma_{\kappa}$  are more or less a constant of  $M_A$ . This is expected since we should only see the hydrodynamic nature of the magnetized turbulence if we are observing it along its mean field direction. We see that the value of  $\langle\kappa\rangle$  arrives at the maximum value allowed in the curvature algorithm (see Section 3.4). This suggests that the measured Alfvénic Mach number is actually the perpendicular Mach number  $M_{A,perp}=M_A\cos\theta$ , where  $\theta$  is the angle between the mean magnetic field and the LOS.

In the case of the power-law tail slope of the pdf, we see that there still exists a power law between the pdf slope and  $M_A$ . One interesting thing to note here is that the values of the power-law tail slope actually become more disperse when the synthetic maps are obtained by being projected perpendicular to the mean magnetic field directions than those in 3D. When we view the numerical cube with its mean field parallel to the LOS, we also see that the pdf tail slope has different responses as a function of  $M_A$  compared to that when  $B \perp$  LOS. By using these tools together, it is possible to extract the Alfvénic Mach number in the range of  $M_A \in (0.2, 1.7)$ .

### 5. Relation of Gradient Curvature, Magnetic Field Line Curvature, and Magnetization

Aside from the curvature of magnetic field lines, we could also apply the curvature technique to a method that could potentially trace magnetic field lines. The VGT (Yuen & Lazarian 2017a, 2017b; Lazarian & Yuen 2018a) is a very powerful technique in probing magnetic field using gradient statistics of turbulence observables. Theoretically for a local magnetic field **B** we expect the term  $B \cdot \nabla v$  to be statistically zero as long as the area of sampling is large enough, which is shown in the series of VGT literature. Under the framework of curvature, we expect to see that the curvature of velocity gradients would be statistically comparable to that of magnetic field curvature. Since we are down-sampling the data with the sub-block averaging (Yuen & Lazarian 2017a), the pdf would not have enough sample to plot even with the smallest block size allowed. As a result, we omit discussion on the pdf tail slope in the sections that involve the block averaging. Here we select a block size of 72 pixels as a case study of how well gradient curvature could represent magnetization.

We show the curvature of magnetic field as probed by the VGT in Figure 4. Notice that the gradient method in the recipe of Yuen & Lazarian (2017a) would introduce natural dispersion, which has been discussed also in Lazarian et al. (2018). In the concept of curvature, that means that the minimum curvature attained by gradients of these observables is not zero, which has been reflected as the "base" of the top-base method in Lazarian et al. (2018). With enough resolution in simulation and statistically sufficient block-sampling, this minimum curvature would eventually go to zero.

While there are different dependencies of the statistical measures, there are few interesting properties in Figure 4 that are consistent with previous sections or works on VGT. For instance, there is a generally growing trend for both  $\langle \kappa \rangle$  and  $\sigma_{\kappa}$ when  $M_A$  increases, which suggests that the gradients of these observables are indeed correlated to the magnetic field curvature. Counting the factor of nonzero minimum curvature for gradients, it is possible to correlate the curvature of gradients of observables to the curvature of magnetic field. Second, it is very apparent that the curvature of intensity gradients is significantly larger than that of the velocity centroid and channel gradients, especially in the case of  $M_{\rm A} < 1$ . This is consistent with the previous VGT finding that centroids are generally better than intensity gradients (Yuen & Lazarian 2017a, 2017b), channels are even better in representing the magnetic field structure compared to centroids and intensity gradients (Lazarian et al. 2018; Hu et al. 2018), and also intensity gradients are affected by shocks and self-gravity (Yuen & Lazarian 2017b; Hu et al. 2019). Third, there is a significant flattening of both  $\langle \kappa \rangle$  and  $\sigma_{\kappa}$  of all three observables as  $M_A \geqslant 1$ . This is because the turbulent scalings are different in the case of  $M_A < 1$  and  $M_A > 1$  (see Lazarian 2006 for a summary of them).

## 6. Contribution of Different Modes toward Curvature of Gradients

The concept of MHD modes is crucial in understanding the geometry of magnetic field lines in interstellar media. In compressible turbulence it is found numerically that Alfvén modes dominate. In the case of 3D MHD compressible turbulence with the mean field being a straight line, the Alfvén mode is believed to be divergence free (Cho & Lazarian 2002; Jungyeon & Lazarian 2003; Lazarian 2006; see also Sections 8.2 and 8.3 for an alternative discussion). The two compressible modes could then be represented by linear combinations of the so-called parallel (to the local magnetic field; see Section 2.1) and perpendicular components of a wavevector. Under this assumption, Jungyeon & Lazarian (2003) developed a technique in obtaining the unit vectors of the three MHD modes and tested the expected dependence theoretically derived in Goldreich & Sridhar (1995) that  $k_{\parallel} \propto k_{\perp}^{2/3}$ . One of the very important discoveries from Jungyeon & Lazarian (2003) is that there is little interference between the incompressible Alfvén modes and the compressible slow and fast modes during the whole simulations, suggesting that the coupling between Alfvén and other modes is weak. The incompressibility of Alfvén mode also suggests that the only way to store energy into Alfvén mode is to bend it, i.e., introduce curvature to it. While it is also possible to bend the other two modes, the compressibility of these modes acts as

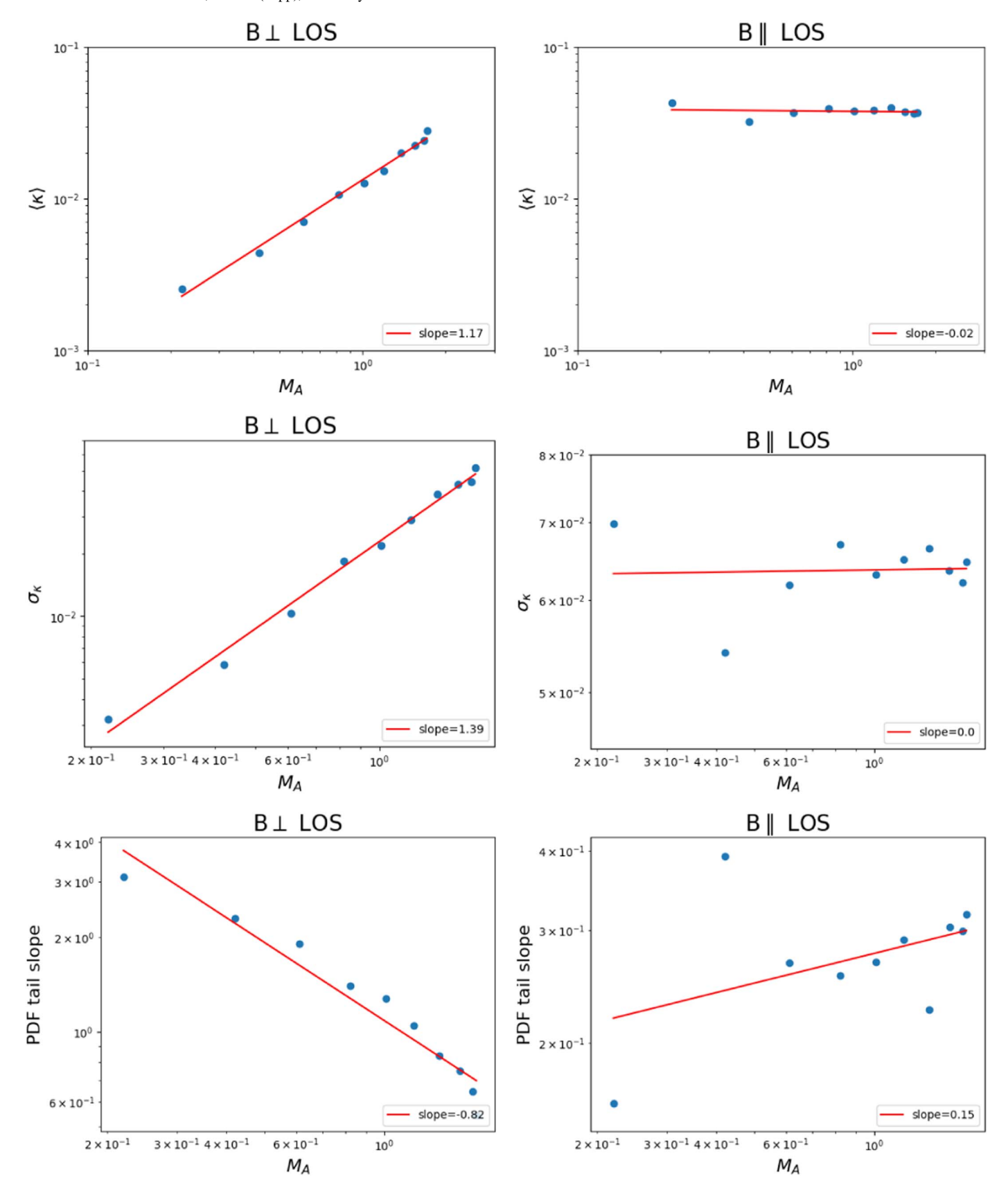


Figure 3. Plot of  $\langle \kappa \rangle$  (top row),  $\sigma_{\kappa}$  (middle row), and (absolute value of) the slope of the pdf tail (bottom row) as functions of  $M_A$  when we project the numerical cube perpendicular to the magnetic field (left column) and parallel to the magnetic field (right column). We provide the slope of the fitting line for each panel.

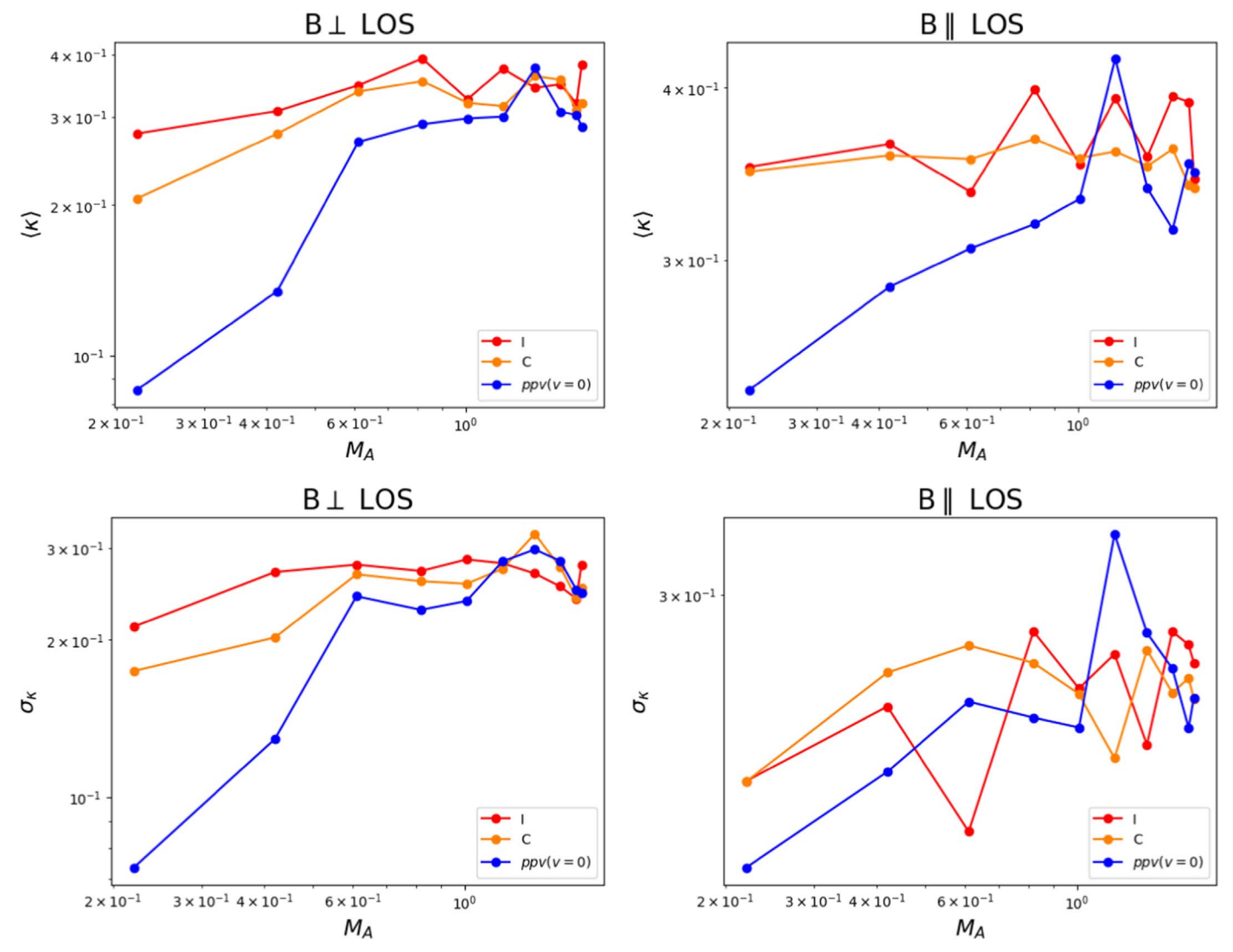


Figure 4. Four panels showing how the curvature of intensity gradients (red), velocity centroid gradients (orange), and velocity channel with  $\nu=0$  (blue) are related to  $M_S$  under three statistical parameters  $\langle \kappa \rangle$  (left column) and  $\sigma_{\kappa}$  (right column) for both  $B\perp$  LOS (top row) and  $B\parallel$  LOS (bottom row). See Section 3.2 for the definition of the observables.

a spring that can absorb energy when bending them. Therefore, it is obvious that Alfvén mode would store much more energy due to curvature than the other two modes. Combined with the fact that Alfvén modes dominate over the two other modes, we expect that the curvature would be mostly contributed by the Alfvén modes. Below we shall examine the velocity gradient curvature induced by different modes as a function of Alfvénic Mach number.

The mode decomposition method for *single-fluid polytropic MHD turbulence* is described in Cho & Lazarian (2002) and further elaborated in Jungyeon & Lazarian (2003). The three MHD modes, namely, the Alfvén, slow, and fast modes, can be decomposed in Fourier space with respect to the local mean magnetic field  $\boldsymbol{B}_0$  by

$$\mathbf{k} = k_{\parallel} \hat{\mathbf{B}}_{0} + k_{\perp} \hat{\mathbf{k}}_{\perp} = k_{\parallel} \hat{\mathbf{k}}_{\parallel} + k_{\perp} \hat{\mathbf{k}}_{\perp}$$

$$\hat{\zeta}_{A} = \hat{\mathbf{k}}_{\perp} \times \hat{\mathbf{k}}_{\parallel}$$

$$\hat{\zeta}_{S} \propto (-1 + \alpha - \sqrt{D}) k_{\parallel} \hat{\mathbf{k}}_{\parallel} + (1 + \alpha - \sqrt{D}) k_{\perp} \hat{\mathbf{k}}_{\perp}$$

$$\hat{\zeta}_{F} \propto (-1 + \alpha + \sqrt{D}) k_{\parallel} \hat{\mathbf{k}}_{\parallel} + (1 + \alpha + \sqrt{D}) k_{\perp} \hat{\mathbf{k}}_{\perp}. \tag{21}$$

These unit vectors are mutually orthogonal and span over  $\mathcal{B}^3$ . The decomposition is valid when the physical scale is larger than the first decoupling scale  $k_{\text{decl.,ni}}$  as neutrals and ions can be considered to be one comoving species instead of two (see Xu et al. 2015, 2016). The decomposition starts to become physically unjustified as between the two decoupling scales  $k_{\text{decl.,ni}} = \gamma_d \rho_i < \gamma_d \rho_n = k_{\text{decl.,in}}$  there are three more damping modes for the two velocities  $v_{i,n}$  that characterize the two-fluid partially coupling MHD equations. In our case we are mostly in the diffuse ISM regime; therefore, we could stick with the single-fluid mode decomposition for the rest of the current section.

The LOS component of the three modes is projected perpendicularly, so that we would not be interfered by the LOS effect (see Section 4). The projection is effectively computing the velocity centroid of these three modes assuming the density as a constant. The assumption is necessary since the density fluctuation corresponding to Alfvén mode is zero, but this is not the case for the slow and fast modes. For a fair comparison we only consider their velocity fluctuations and see

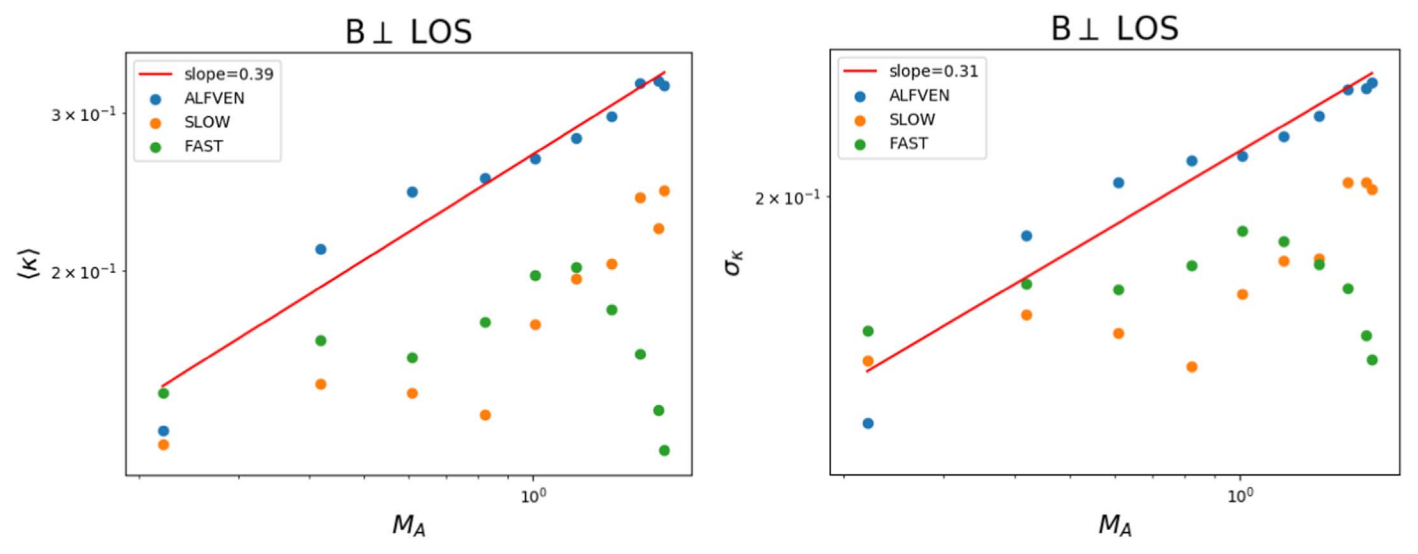


**Figure 5.** Two panels showing how  $\langle \kappa \rangle$  and  $\sigma_{\kappa}$  of the gradients of Alfvén (blue), slow (orange), and fast (green) modes behave as a function of  $M_A$ . We also provide the fitting line for the Alfvén mode, which is a more apparent power-law relation in these two panels.

how the three modes would behave. In this scenario we find that a block size of 18 pixels would fulfill the block-averaging condition (Yuen & Lazarian 2017a).

Figure 5 shows how  $\langle \kappa \rangle$  and  $\sigma_{\kappa}$  of the gradients of Alfvén (blue), slow (orange), and fast (green) modes behave as a function of  $M_A$ . We also provide the fitting line for the Alfvén mode, which is a more apparent power-law relation in these two figures. We can immediately see a few things from these figures. First, the result from Figure 5 shows that Alfvén mode indeed has a higher curvature value compared to the other two modes, with the only exception being the  $M_A = 0.2$  case (huge-0). The reason for the latter is that in the case of very low  $\beta$  the compression perpendicular to the LOS is simply much stronger. As a result, one could see dominance of fast modes that would be almost  $||k_{\perp}|$  in the case of  $M_A = 0.2$  since the respective  $\beta$  value is  $\ll 1$  (see Table 1 and also the Appendix of Jungyeon & Lazarian 2003). Another thing that we see from Figure 5 is that, while there is no apparent power-law fit that could be found between both  $\langle \kappa \rangle$  and  $\sigma_{\kappa}$  to  $M_A$  for the two compressible modes, there exists a nicely fit power law for Alfvén mode to  $M_A$  but with a much flatter slope, contrary to the absence of power law in what we see from Section 5. The filtering of slow and fast modes is well known to improve hunting of anisotropy (Kowal & Lazarian 2010) and also performance of the VGT (Lazarian et al. 2017, 2018). The existence of the power law on Alfvén modes to  $M_A$  would indicate that the magnetization could be estimated if the compressible modes are filtered.

#### 7. Application to Observational Data

We test our method in Section 4 in the recently available Planck data (Planck Collaboration et al. 2018). We use the 353 GHz full-sky map (R3.01) and obtain the polarization angle  $\phi = 0.5a\tan_2(U/Q)$  from the data. We then compute the circular dispersion of polarization angles  $\delta\phi$  and the curvature quantities  $\langle\kappa\rangle$  and  $\sigma_{\kappa}$  as proposed in Section 4. They are all computed in a block size of 4.17 deg<sup>2</sup>. Since these three parameters all increase with  $M_A$ , we could see whether the approach employing curvature is useful. We do this by comparing the spatial correlation of the curvature statistics to that of the dispersion of angles.

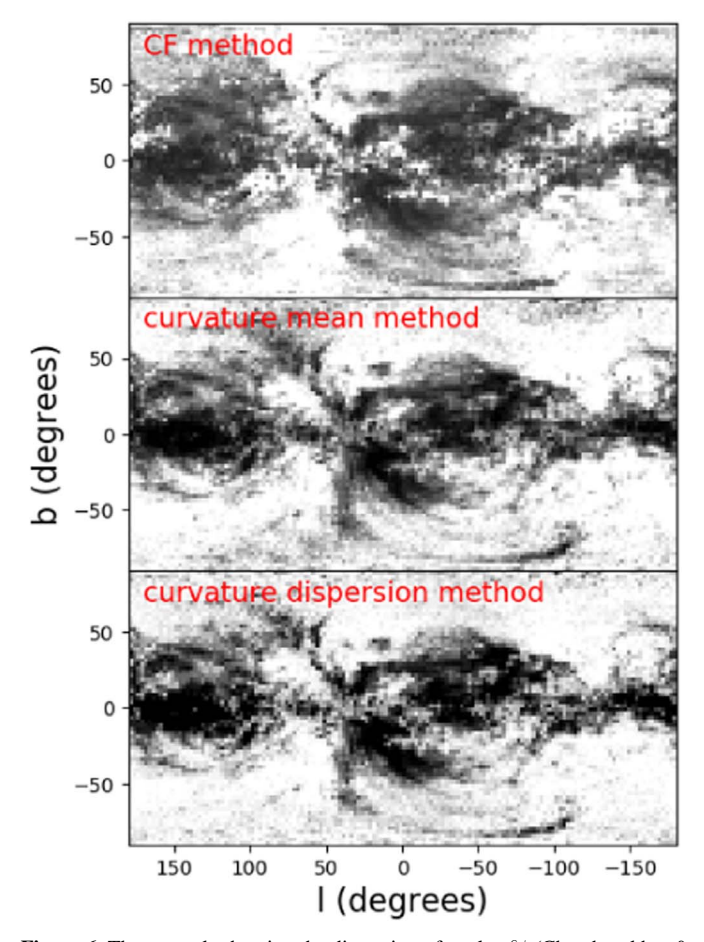


**Figure 6.** Three panels showing the dispersion of angles  $\delta\phi$  (Chandrasekhar & Fermi 1953; top panel) and the mean  $\langle\kappa\rangle$  and dispersion of curvature  $\sigma_\kappa$  method (middle and bottom panels; Section 4) with a block size of 4.17 deg<sup>2</sup>. The color scale is set such that a lighter color indicates a larger value of that quantity and scales up within one standard deviation.

Figure 6 shows how these parameters are distributed in the full sky. One could see visually that these three methods are spatially correlated. In the following we employ the normalized cross-correlation function (NCC) NCC(a, b) = Cov(a, b)/ $\sigma_a\sigma_b$ ,

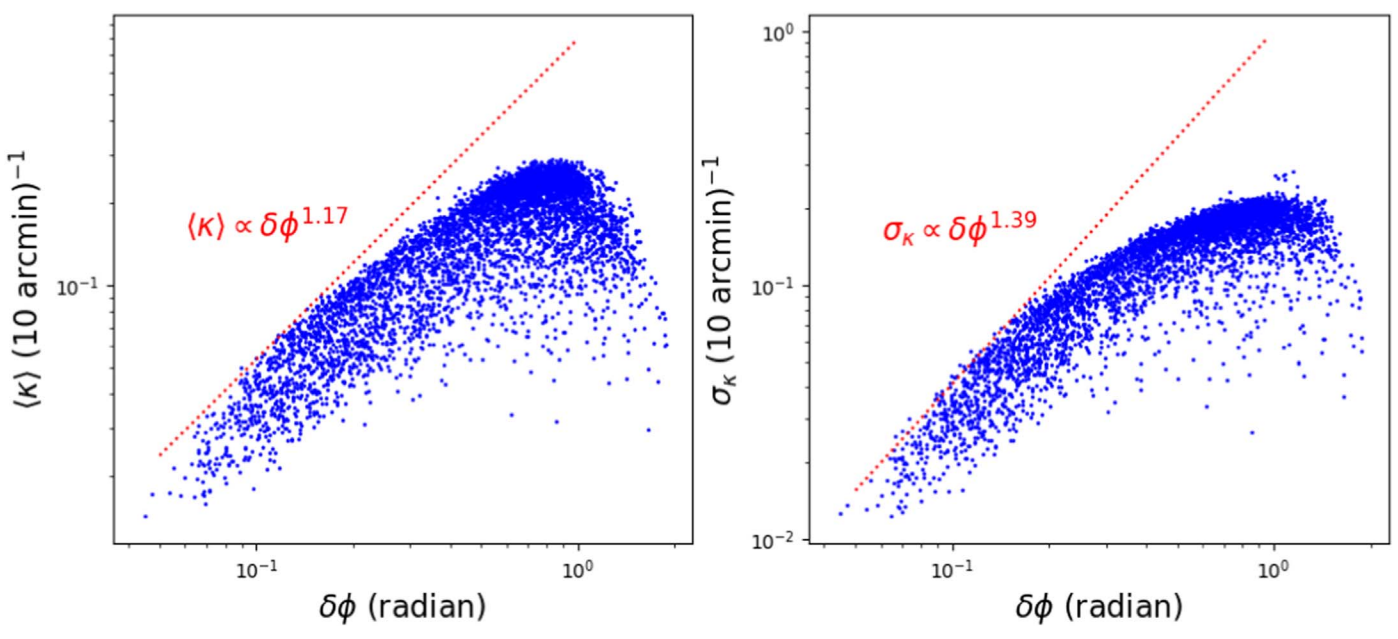


Figure 7. Two panels showing the scatter plot of  $\langle \kappa \rangle - \delta \phi$  (left) and  $\sigma_{\kappa} - \delta \phi$  (right) using the 353 Ghz Planck Polarization data at a block size of 4.17 deg<sup>2</sup>. The two trend lines are added according to the prediction in Section 4.2.

where Cov is the covariance function, as a tool to compare the similarity of the two 2D maps. The NCC has a range of [-1, 1], with NCC > 0 meaning that the two maps have positive correlation and vice versa. We compute the NCC function between the dispersion of angles to both mean  $\langle \kappa \rangle$  and dispersion of curvature  $\sigma_{\kappa}$  and see that

$$NCC(\delta\phi, \langle\kappa\rangle) \sim 0.63$$
  
 $NCC(\delta\phi, \sigma_{\kappa}) \sim 0.76.$  (22)

We would also compare the two measurements locally. We know that  $\delta\phi\propto M_{\rm A}$ , and from Section 4.2 we know that  $\langle\kappa\rangle\propto M_{\rm A}^{1.17}$  and  $\sigma_\kappa\propto M_{\rm A}^{1.39}$ . Therefore, we expect  $\langle\kappa\rangle\propto\delta\phi^{1.17}$  and  $\sigma_\kappa\propto\delta\phi^{1.39}$ . Figure 7 shows how the scatter plot of  $\langle\kappa\rangle$  (left) and  $\sigma_\kappa$  (right) behaves with respect to  $\delta\phi$ . We added the trends as predicted in Section 4.2 and see that the trend lines in both figures predict the shape of both scatter plots when  $\delta\phi<0.2$ , which is consistent with the numerical exploration in Section 4.2. For  $\delta\phi>0.2$  rad  $\sim11^\circ.4$ , both figures have a significant deviation from the curvature statistics. However, generally both  $\langle\kappa\rangle$  and  $\sigma_\kappa$  have a positive relation to  $\delta\phi$ . This shows that the statistical measure of  $\kappa$  is a valid measurement of magnetization.

#### 8. Discussion

### 8.1. The Use of Torsion in Studying Magnetic Field

Aside from curvature, torsion is also a very important geometric quantity for the magnetic field. While the use of torsion is less popular in literature, we should not underestimate the importance of torsion since it records how sharply the magnetic field lines twist out of the plane of curvature. The concept of torsion is especially useful when we are dealing with the natural oscillation modes in magnetized turbulence, namely, the fast, slow, and Alfvénic modes (see Biskamp 2003; Jungyeon & Lazarian 2003). In fact, when a magnetic field mode is

propagating along some directions, the speed of rotation of the eddy that is *along the azimuthal direction* of the propagating directions records the torsion of the mode. The signature of magnetic field rotates when propagating is especially important when we are studying modes in MHD turbulence.

Curvature and torsion could be easily visualized when the magnetic field lines have some special geometry. For instance, if the magnetic field line could be parameterized by a circular helix  $L_B(t) = (a\cos(t), a\sin(t), bt)$ , then the curvature and torsion of this magnetic field line are simply  $\kappa = a/\sqrt{a^2 + b^2}$  and  $\tau = b/\sqrt{a^2 + b^2}$ , respectively. From Equation (2) we could have a formula for the signed torsion:

$$\tau = \hat{b} \cdot \frac{d\hat{n}}{ds}.\tag{23}$$

The estimation of curvature and torsion would also be very important in advancing the VGT since essentially Equation (2) describes the behavior of first three derivatives of the orientation of magnetic fields. In the VGT we approximated  $\hat{t}$  by block averaging (Yuen & Lazarian 2017a). The curvature could be possibly approximated by the magnetization technique by Lazarian et al. (2018) with Figure 1 in 3D or Figure 3 in 2D. Numerically if we know both the tangent and curvature, we could then solve the magnetic field line equation by Equation (2) and Equation (15). By studying the properties of the torsion field, we would know what the second derivative of the orientation of magnetic field would look like, and that would provide us with a geometrically more plausible way of reconstructing the magnetic field directions.

#### 8.2. Divergence of Alfvén Mode

One of the very important applications of the Frenet–Serret frame derived from the magnetic field line is to recognize how the three MHD modes are related to the curvature and torsion of magnetic lines. Below we shall discuss how the three MHD modes would be related to the local Frenet-Serret frame of magnetic field by the theory of MHD turbulence (Goldreich & Sridhar 1995; Lazarian & Vishniac 1999). In the case of Jungyeon & Lazarian (2003) decomposition the mean field has to be locally a straight line. 10 In this scenario there is an ambiguity in defining the directions of both  $\hat{n}$  and  $\hat{b}$ . One could simply assign the Alfvén wave unit vector to be along one of these directions. However, in the case of a mean magnetic field with nonzero curvature, the effect of frame changes in the local regions has to be taken into account, and we have to drop some assumptions that were valid in usual compressible 3D magnetized turbulence. For instance, the assumption that Alfvén mode is divergence free is not correct when the local mean field has nonzero curvature. Southwood & Saunders (1985) propose that the Alfvén mode has a nonzero divergence related to the curvature of the mean magnetic field:

$$\nabla \cdot \hat{\zeta}_{A} \sim \kappa \hat{\zeta}_{A} \cdot \hat{n}, \tag{24}$$

where  $\hat{\zeta}_{\rm A}$  is the Alfvén mode unit displacement vector. Following Southwood & Saunders (1985), there is a source term for the slow wave equation to be proportional to  $\kappa \hat{\zeta}_A \cdot \hat{n}$ , while the Alfvén mode wave equation has a similar term that is  $\propto \kappa \hat{n}$ . Physically the bent magnetic field would induce a change of fluid element volume toward the center of curvature, whose size is proportional to  $\kappa$ . As a result, the plasma pressure due to the compression of volume is changed under this magnetic field geometry, which would drive the slow mode to oscillate along with the azimuthal direction of Alfvén mode. However, the Alfvén mode in this situation is no longer solenoidal (see Equation (23) or Figure 3 of Southwood & Saunders 1985), which is different from the case when we perform mode decomposition with a mean field with  $\kappa = 0$  (see Jungyeon & Lazarian 2003 for a discussion of MHD modes). Unlike Jungyeon & Lazarian (2003), where the mean magnetic field was approximated by a straight line, the study in Southwood & Saunders (1985) points out that in the presence of uniform nonzero curvature magnetic field the transfer of energy between Alfvén and slow modes increases. This effect is, however, reduced by the Alfvénic cascade happening in one eddy turnover time, which makes the effect important only when the curvature is comparable to the wavenumber of the perturbations under consideration.

# 8.3. The Picture of MHD Modes under Strongly Curved Magnetic Field

Equation (24) suggests that the Alfvén mode wavevector, which lies on the plane spanned by the normal and the binormal vector, would rotate as a function of curvature with its rotation axis aligned with the tangent vector  $t = B_0$ . Equation (24) suggests that if  $\lambda_{\perp}$  is the perpendicular

wavelength and  $\phi_k = \cos^{-1}(\hat{k} \cdot \hat{b})$ , then the angle of rotation  $\phi_A$  of the Alfvén mode with respect to the tangent vector is given by

$$\cos \phi_{\rm A} \sim \frac{\cos \phi_k}{\lambda_{\parallel} \kappa}.$$
 (25)

Therefore, for a magnetized turbulent system with a nonzero mean magnetic field curvature, one could (1) compute the components of wavevector with respect to the Frenet–Serret frame, (2) compute the orientation of MHD modes according to Jungyeon & Lazarian (2003) and represent these eigenvectors by the Frenet–Serret frame, and (3) rotate the three MHD mode vectors with the rotation matrix  $R(\hat{t}, \phi_A)$ , where  $\hat{t}$  is the rotation axis. This method allows one to use the formulation of Jungyeon & Lazarian (2003) to compute the MHD modes.

### 8.4. Importance of Gravity to Magnetic Field

The important insight of increasing coherent coupling between Alfvén and slow modes in the presence of nonzero curvature mean field suggests that using the concept of modes in systems that have nonzero mean magnetic field curvature should be done with caution. In Section 2, we see that the curvature naturally introduces a length scale related to the radius of curvature  $r_c = \kappa^{-1}$ . Above the aforementioned length scale Alfvén and slow modes are coupled, while below that they act independently. In the case that there are no external forces holding the magnetic field, the magnetic field curvature would restore to infinity, so that the magnetic field will become a straight line when the magnetic energy from the curvature is all transferred to the dissipation of Alfvén and slow modes.

However, in real astrophysical scenarios, there are external forces that can keep magnetic fields bent. One of the best examples would be self-gravity. It is shown observationally by Li et al. (2015) that the curvature of magnetic field could be used in estimating the magnetic field strength on a self-similar molecular cloud, suggesting that the curvature of magnetic field does not dissipate to Alfvén and slow mode driving in a self-gravitating system. In fact, it is easy to imagine that the gravitational field provides support for the curvature of magnetic field. Following Li et al. (2015), for a spherical self-gravitating object of constant density  $\rho$ , radius R, and mean magnetic field strength R, along the normal direction of magnetic field,

$$\frac{B^2}{R} \sim \frac{4\pi}{3} G \rho^2 R,\tag{26}$$

for which one would have  $\kappa$   $(v_A t_{ff}) \sim 1$ , where  $t_{ff} \sim (G\rho)^{-1/2}$  is the freefall time. When  $r_c = \kappa^{-1} \gg v_A t_{ff}$ , magnetic field dominates over gravity, and vice versa. This suggests that curvature could be supported by gravity if Equation (26) is satisfied.

Under the scenario that  $\kappa(v_A t_{ff}) \sim 1$ , the gravitational energy would become the primary energy source in driving both (non-incompressible) Alfvén and slow waves. When the density of the self-gravitating object increases, it is expected to have a runoff effect by having a larger curvature and a much stronger coupling between the Alfvén and slow modes. Moreover, the dependence of curvature on magnetic field changes from  $\kappa \propto B^{-2}$  in nongravitating systems to  $\kappa \propto \rho B^{-1}$  in self-gravitating systems.

<sup>&</sup>lt;sup>10</sup> The "locality" issue in Jungyeon & Lazarian (2003) is hard to implement in numerical simulations. In theory, if one could sample a small enough space in the turbulence cube provided that the space has enough resolution for the Fourier transform, the locality could be obtained within that small enough space, which is the essence of the Jungyeon & Lazarian (2003) decomposition. However, due to the restrictions of resolutions, the statistics of a very small region in numerical simulations are dominated by dissipations. Kowal & Lazarian (2010) later use the method of wavelets to localize the Jungyeon & Lazarian (2003) formalism.

### 9. Conclusions

The use of geometrical properties of magnetic field lines and interaction with magnetized turbulence would help us both advance the theory of MHD turbulence and also introduce ways to study magnetic fields in observation. In this work, we explore the statistical properties of magnetic field line curvature  $\kappa$  in compressible magnetized turbulence. To summarize:

- 1. We propose an algorithm in computing the curvature of both gradients of a scalar field and a vector field (Section 3.4).
- 2. We study the mean value and the standard deviation of magnetic field line curvature and identify the power-law relation of the two quantities with the magnetization (Section 4.2).
- 3. We also obtain the power-law relation of the spectral index of the histogram of curvature with the Alfvénic Mach number (Section 4.2).
- 4. The power laws can also be seen in observation with the exception of degenerate cases when mean magnetic field is either parallel or perpendicular to the LOS (Section 4.2).
- 5. The curvature method can be used in advancing the VGT and predicts the magnetization based on the gradients of observables (Section 5).
- 6. The MHD mode analysis shows that Alfvén mode is the dominant curvature contribution toward the magnetic field lines traced by velocity gradients (Section 6).
- 7. We test our prediction of power law in Section 4.2 in observation and see the same relation of  $\kappa$  to  $\delta \phi$  when the latter is small (Section 7).

8. We discuss the modifications of the physics of Alfvén modes when the background magnetic field has significant curvature (Section 8.2).

K.H.Y. acknowledges Korea Astronomy and Space Science Institute on 2018 November for hospitality in inspiring the curvature algorithm. We acknowledge the support of NSF AST 1816234 and NASA TCAN 144AAG1967. A.L. thanks the Center for Computational Astrophysics (CCA) for its hospitality. This research used resources of both the Center for High Throughput Computing (CHTC) at the University of Wisconsin and the National Energy Research Scientific Computing Center (NERSC), a U.S. Department of Energy Office of Science User Facility operated under contract No. DE-AC02-05CH11231, as allocated by TCAN 144AAG1967.

## Appendix The Convergence Test for the Curvature Algorithm

In this section we perform a convergence test and see whether the algorithm that we developed in Section 3.4 would converge as we change the only parameter dt in the algorithm. We test a wide range of the step size, and Figure A1 shows the value of curvature in four randomly drawn pixels in our simulations as a function of step size. We can see that the estimated curvature value is basically constant within the range of the dt that we selected. We therefore believe that our method of obtaining curvature is robust when an appropriate dt is selected.

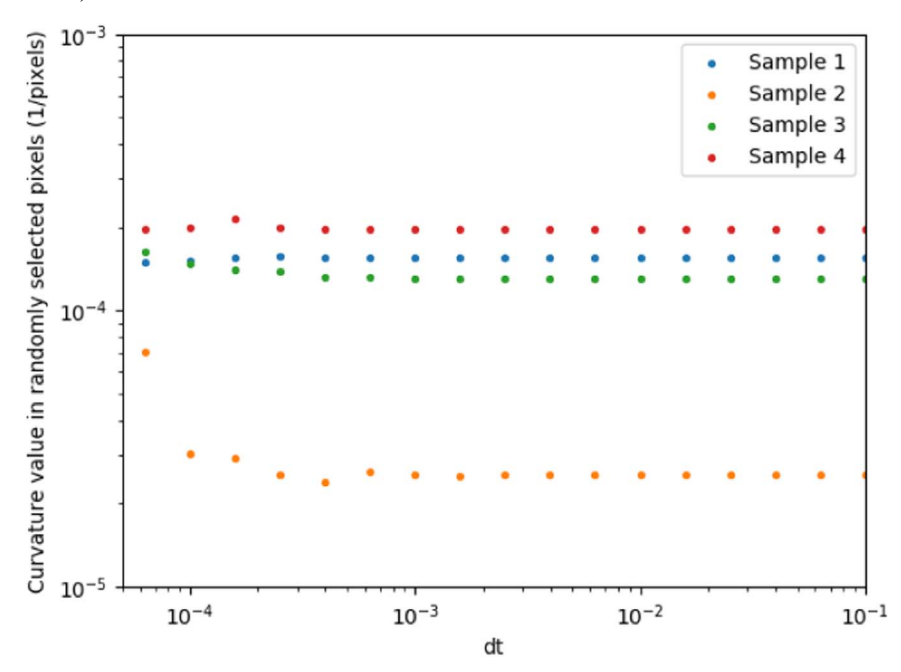


Figure A1. Plot showing how the curvature value for four randomly drawn pixels in the simulation huge-0 depends on the step size dt.

#### ORCID iDs

Ka Ho Yuen https://orcid.org/0000-0003-1683-9153 Alex Lazarian https://orcid.org/0000-0002-7336-6674

#### References

```
Armstrong, J. W., Rickett, B. J., & Spangler, S. R. 1995, ApJ, 443, 209
Begum, A., Chengalur, J. N., & Bhardwaj, S. 2006, MNRAS, 372, L33
Beresnyak, A., & Lazarian, A. 2019, Turbulence in Magnetohydrodynamics
  (Berlin: De Gruyter)
Beresnyak, A., Lazarian, A., & Cho, J. 2005, ApJL, 624, L93
Biskamp, D. 2003, Magnetohydrodynamic Turbulence (Cambridge: Cambridge
   Univ. Press), 310
Brandenburg, A., & Lazarian, A. 2013, SSRv, 178, 163
Braun, W., de Lillo, F., & Eckhardt, B. 2006, JTurb, 7, 62
Bruno, R., & Carbone, V. 2013, LRSP, 10, 2
Callen, J. D., Hegna, C. C., & Sovinec, C. R. 2003, in APS Meeting DPP03,
   5th Annual Meeting of the Division of Plasma Physics (Washington, DC:
   APS), QP1.110
Chandran, B. D. G. 2000, PhRvL, 85, 4656
Chandrasekhar, S., & Fermi, E. 1953, ApJ, 118, 113
Chepurnov, A., & Lazarian, A. 2010, ApJ, 710, 853
Cho, J., & Lazarian, A. 2002, PhRvL, 88, 245001
Cho, J., Lazarian, A., & Vishniac, E. 2001, ApJ, 564, 291
Cho, J., Lazarian, A., & Vishniac, E. T. 2002, ApJ, 564, 291
Cho, J., & Vishniac, E. T. 2000, ApJ, 539, 273
Deshpande, A. A., Dwarakanath, K. S., & Goss, W. M. 2000, ApJ, 543, 227
Dickey, J. M., McClure-Griffiths, N. M., Stanimirović, S., Gaensler, B. M., &
   Green, A. J. 2001, ApJ, 561, 264
Draine, B. T. 2009, in ASP Conf. Ser. 414, Cosmic Dust-Near and Far, ed.
   T. Henning, E. Grün, & J. Steinacker (San Francisco, CA: ASP), 453
Elmegreen, B. G., & Scalo, J. 2004, ARA&A, 42, 211
Farmer, A. J., & Goldreich, P. 2004, ApJ, 604, 671
Fissel, L. M., Ade, P. A. R., Angilè, F. E., et al. 2016, ApJ, 824, 134
Goldreich, P., & Sridhar, S. 1995, AJ, 438, 763
Goldstein, M. L., Roberts, D. A., & Matthaeus, W. H. 1995, ARA&A, 33, 283
González-Casanova, D. F., & Lazarian, A. 2017, ApJ, 835, 41
Green, D. A. 1993, MNRAS, 262, 327
Higdon, J. C. 1984, ApJ, 285, 109
Hu, Y., Yuen, K. H., & Lazarian, A. 2018, MNRAS, 480, 1333
Hu, Y., Yuen, K. H., & Lazarian, A. 2019, ApJ, 884, 137
Jokipii, J. R. 1966, ApJ, 146, 480
Jungyeon, C, & Lazarian, A. 2003, MNRAS, 345, 325
Kadoch, B., Del-Castillo-Negrete, D., Bos, W. J. T., et al. 2011, PhRvE, 83,
```

```
Khalil, A., Joncas, G., Nekka, F., Kestener, P., & Arneodo, A. 2006, ApJS,
   165, 512
Kowal, G., & Lazarian, A. 2010, ApJ, 720, 742
Lazarian, A. 2006, ApJ, 645, L25
Lazarian, A. 2016, ApJ, 833, 131
Lazarian, A., & Esquivel, A. 2003, ApJL, 592, L37
Lazarian, A., & Pogosyan, D. 2004, ApJ, 616, 943
Lazarian, A., & Pogosyan, D. 2006, ApJ, 652, 1348
Lazarian, A., & Vishniac, E. T. 1999, ApJ, 517, 700
Lazarian, A., & Yan, H. 2014, ApJ, 784, 38
Lazarian, A., & Yuen, K. H. 2018a, ApJ, 853, 96
Lazarian, A., & Yuen, K. H. 2018b, ApJ, 865, 59
Lazarian, A., Yuen, K. H., Ho, K. W., et al. 2018, ApJ, 865, 46
Lazarian, A., Yuen, K. H., Lee, H., & Cho, J. 2017, ApJ, 842, 30
Lazarian, A., Yuen, K. H., & Pogosyan, D. 2020, arXiv:2002.07996
Li, H.-B., Yuen, K. H., Otto, F., et al. 2015, Natur, 520, 518
Mac Low, M.-M., & Klessen, R. S. 2004, RvMP, 76, 125
Maron, J., & Goldreich, P. 2001, ApJ, 554, 1175
Matthaeus, W. H., Dmitruk, P., & Milano, L. J. 2002, PhPl, 9, 2440
Matthaeus, W. H., Ghosh, S., Oughton, S., et al. 1996, JGR, 101, 7619
Matthaeus, W. H., Montgomery, D. C., & Goldstein, M. L. 1983, PhRvL,
McKee, C. F., & Ostriker, E. C. 2007, ARA&A, 45, 565
Montgomery, D. 1982, PhST, T2A, 83
Montgomery, D., & Turner, L. 1981, PhFl, 24, 825
Newcomb, W. A. 1958, AnPhy, 3, 347
Ouellette, N. T., & Gollub, J. P. 2007, PhRvL, 99, 194502
Ouellette, N. T., & Gollub, J. P. 2008, PhFl, 20, 064104
Ouellette, N. T., Xu, H., Bourgoin, M., et al. 2006, NJPh, 8, 102
Padoan, P., Juvela, M., Kritsuk, A., & Norman, M. L. 2006, ApJL, 653,
  L125
Planck Collaboration, Akrami, Y., Arroja, F., et al. 2018, arXiv:1807.06205
Shebalin, J. V., Matthaeus, W. H., & Montgomery, D. 1983, JPIPh, 29,
Southwood, D. J., & Saunders, M. A. 1985, P&SS, 33, 127
Straus, J. M., & Schulz, M. 1976, JGR, 81, 5822
Tu, C.-Y., & Marsch, E. 1995, SSRv, 73, 1
Xu, H., Ouellette, N. T., & Bodenschatz, E. 2007, PhRvL, 98, 050201
Xu, S., & Lazarian, A. 2018, ApJ, 868, 36
Xu, S., Lazarian, A., & Yan, H. 2015, ApJ, 810, 44
Xu, S., Yan, H., & Lazarian, A. 2016, ApJ, 826, 166
Yan, H., & Lazarian, A. 2008, ApJ, 673, 942
Yang, Y., Wan, M., Matthaeus, W. H., et al. 2019, PhPl, 26, 072306
Yuen, K. H., Chen, J., Hu, Y., et al. 2018, ApJ, 865, 54
Yuen, K. H., & Lazarian, A. 2017a, ApJL, 837, L24
Yuen, K. H., & Lazarian, A. 2017b, arXiv:1703.03026
Zank, G. P., & Matthaeus, W. H. 1992, JGR, 97, 17189
```